Effects of suppressing the 3D separation on the rear slant on the flow structures around an Ahmed body

A. Thacker *, S. Aubrun, A. Leroy, P. Devinant

Laboratoire PRISME, Université d'Orléans, 8, rue Léonard de Vinci, F-45072 Orléans cedex 2, France

ARTICLE INFO

ABSTRACT

This work considers separated flow past ground vehicles. It consists in analyzing the effect of canceling the separation on the rear slant of an Ahmed body (inclined at 25°) on the different structures developing in the wake. In order to better understand the flow features when canceling separation by means of flow control for drag reduction, two model configurations were used: one with a sharp edge at the connection between the roof and the rear slant and the second one with a rounded edge preventing the rear slant separation. The different wake features were analyzed experimentally and compared for both configurations. Using PIV measurements, this study focuses especially on the longitudinal vortices developing at each side of the Ahmed body. The comparison between the two configurations showed a drag discrepancy of 10% while the lift level remains unchanged. The absence of the separation bubble on the rear window mainly affects the near rear wake that strongly contributes to the weaker drag level. Moreover, results showed that the absence of this separation does not impact on the mean locations of the lateral longitudinal vortices but more specifically on their vortical center intensity.

© 2012 Elsevier Ltd. All rights reserved.

1. Introduction

It is commonly accepted that flow control techniques can contribute to reducing aerodynamic drag in automotive applications, particularly in the case of interurban travel (Gilliéron and Kourta, 2008). However, flow control is not yet integrated in ground vehicles since this requires a higher maturity of the different technologies and a better knowledge of the physical mechanisms responsible for control efficiency. Working on both aspects will lead to an optimization of the control concepts. Despite recent experimental and numerical work on this subject (Lienhart and Becker, 2003; Krajnovic and Davidson, 2005; Serre et al., in press, Vino et al., 2005), it is still necessary to update knowledge on ground vehicle aerodynamics by means of steady and unsteady information on the drag sources such as 3D separation zones and vortical structures encountered on 3D bluff bodies. Since a real ground vehicle has a very complex shape, a compromise has been found through the design of the Ahmed body (Ahmed et al., 1984). This generic shape is considered to have a similar near-wake to that of a real ground vehicle since it generates the same flow structures. Depending on the chosen slant angle of the rear window, the combination of three features constitute this complex flow: two longitudinal vortical structures,

a 3D separation bubble on the rear window and a 3D wake located at the rear base. The particular case of a 25° slant angle is one of the most complex configurations in modeling flow at the rear of common fastback vehicles since it possesses simultaneously the three features described above. In this configuration each feature contributes to the drag balance: 12% for the longitudinal vortical structures, 34% for the 3D separation bubble, and 44% for the 3D wake behind the rear base (and 10% for others such as viscous drag, forebody contribution) (Leclerc, 2008). Moreover, it is expected that reducing or suppressing one of these structures may modify the others, and that the drag under flow control may not be a straight substraction of the drag contribution of the suppressed structure. Consequently, the properties of the flow under control also need to be studied. In this context, the present study focuses on the effects of suppressing the rear window 3D separation on the other structures composing the Ahmed body near-wake for a 25° rear slant configuration. To obviate the impact of the actuation properties and their specific action mechanisms, the suppression of the separation bubble is obtained by increasing the local radius of curvature of the edge between the roof and the rear window. The near-wake properties are then compared for two distinct models, the first one having a sharp edge between the roof and the rear window, and the second one having a rounded edge. Aerodynamic loads, wall pressure distributions, friction line visualizations and PIV velocity fields are performed to determine the discrepancies between the two configurations. Particular attention is paid to

---

* Corresponding author. Tel.: +33 2 38494351.
E-mail address: adrien.thacker@univ-orleans.fr (A. Thacker).

the influence of the separation bubble suppression on the steady and unsteady behavior of the longitudinal vortical structures.

2. Experimental set-up

Two Ahmed body models with a slant angle of 25° between the roof and the rear window were built at a geometric scale of 1:1 (Fig. 1). One model has a sharp edge between the roof and the slanted surface, whereas the second model has a rounded edge, with an 80 mm radius of curvature (Fig. 2). This radius of curvature is a 1/5 scale of the radius that is commonly found on real scale fastback ground vehicles (400 mm). Moreover, it ensures a fully attached flow on the rear window, as detailed in the results section. Fig. 2 presents the reference frame for the two model configurations. The $X=0$ reference for the rounded edge is located at the intersection of the rear window plane and the roof plane.

The experiments were run in the "Lucien Malavard" wind tunnel of the PRISME Laboratory, University of Orléans. The test section is 2 m high, 2 m wide and 5 m long. The maximum freestream velocity in the test-section is 60 m/s, the freestream turbulence intensity is below 0.3% and the mean flow homogeneity is 0.5% along a transverse distance of 1200 mm. The model is fixed on a 6-axis aerodynamic balance by means of four cylindrical feet (30 mm in diameter) attached to a horizontal metal frame connected to the balance with a 30 mm diameter mast. As an insert, this frame is part of a 2 m wide and 3 m long

Fig. 1. Ahmed body model with a slant angle of 25° at a geometric scale of 1:1.

Fig. 2. Sharp- and rounded-edge configurations between the roof and the rear window.

flat plate located 480 mm above the floor of the wind tunnel; however, the frame is only connected to the balance and not to the flat plate, so as not to transmit any forces to the plate. The use of the flat plate enables the development of a new, thin, boundary layer upstream and underneath the model. The flat plate has an elliptical leading edge and a controllable trailing edge flap which allows the suppression of any pressure gradient in the test section. For a freestream velocity of 30 m/s, the boundary layer thickness on the flat plate just upstream of the model is 20 mm, whereas the ground clearance of the model is 50 mm and the boundary layer at the edge between the roof and the slanted surface is turbulent and is 17 mm thick.

Friction line visualizations on the slanted edge and on the rear base were performed using a viscous coating made of oleic acid, dodecane, silicon oil and titanium dioxide (Anne-Archard et al., 2006). The wall was coated with the mixture using a brush; the model was then exposed to a constant wind until the friction lines became visible (a few minutes).

Static pressure measurements were performed simultaneously at 48 locations distributed all over the rear window with a PSI 8400 multi-scan system. Two ESP-scanners with 32 and 16 channels were used; their full ranges are 1 and 0.3 psid, respectively. The measurement accuracy given by the manufacturer is 0.1% of the full scale range. The scanners were calibrated from 0 to 0.3 psid before each measurement. Plastic tubing 150 mm long with an inner diameter of 1 mm, connects each pressure transducer to the static pressure tap, giving a natural gain of 1.05 at 100 Hz (based on linear acoustic theory, Bergh and Tijdeman, 1965). The samples were taken over a period of 180 s with a sampling frequency of 400 Hz. The reference pressure is the static pressure P_0 measured by the Pitot tube located right above the model, 300 mm from the wind tunnel roof, in the freestream flow. The dynamic pressure $P_{stagnation}-P_0 = 1/2\rho U_0^2$ measured by the Pitot tube was acquired through a differential pressure transducer DRUCK 0-5000 Pa and through one channel of one ESP-scanner. The wall pressure coefficient is the ratio between the differential pressure measured at the wall P_w-P_0 and the dynamic pressure measured by the Pitot tube:

$$C_p = \frac{P_w-P_0}{1/2\rho U_0^2} \tag{1}$$

Aerodynamic loads were measured with a 6-axis balance located below the test section. The precision of the balance is estimated to be 0.16 N and 0.48 N for the drag and lift components, respectively. The sampling frequency was fixed at 100 Hz, and 6000 samples were acquired for each configuration.

Two-component PIV measurements were performed in the vertical plane of symmetry of the body (XZ sheets at $Y=0$), on the rear window and in the near wake. An Nd :Yag laser (QUANTEL ultra 200) generating two pulses of 200 mJ each at a wavelength of 532 nm was located above the test section. A streamwise slit in the test-section roof enables the vertical laser light sheet to reach the model. The optical set-up was chosen to generate a sheet as thin as possible (about 1 mm) in the proximity of the model. Images were captured with a CCD TSI Power View Plus camera (2048 × 2048 pixels) located outside the test section, on one side of the wind tunnel. The complete tunnel circuit was seeded with micro-sized droplets of olive oil generated by a PIVTEC seeding system. The laser and the camera were synchronized by a TSI synchronizer and image processing was performed using Insight3G software by TSI. The PIV image dimensions were 270 mm × 270 mm and interrogation windows of 32 × 32 pixels were used with an overlap of 50% to obtain the velocity field (space resolution $\delta x = 2.1$ mm). One hundred pairs of independent images were captured for each tested configuration with a sampling frequency of 5 Hz. This leads to an RMS error of the
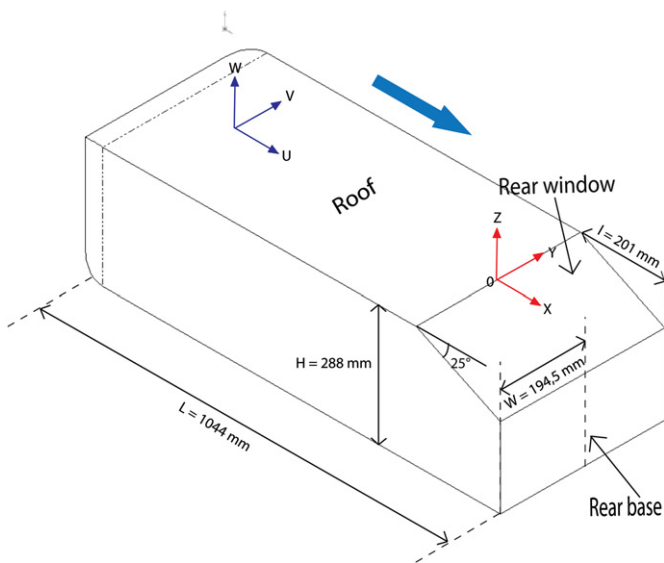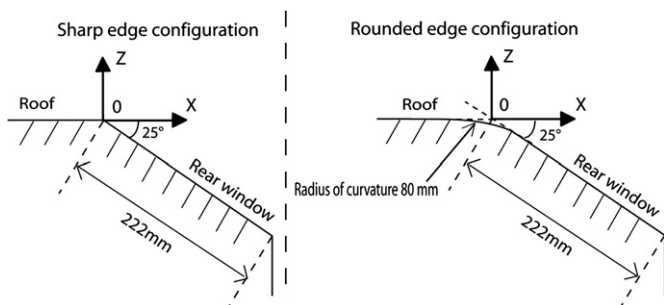
time averaged velocity of 7.8% with a 95% confidence interval (Benedict and Gould, 1996) in the worst case (highest turbulence intensity 40%).

To measure the velocity field through the longitudinal vortical structures (YZ sheets from $X=0$ to $X=290$ mm every $\delta X=10$ mm), the laser light sheet is normal to the freestream direction and the light source is located outside the test section, on one side of the wind tunnel. The camera is located inside the wind tunnel and is fixed on a streamlined mast at a downstream distance of 1200 mm from the model, which corresponds to 17 times the camera dimensions. The PIV image dimensions were 230 mm × 230 mm and interrogation windows of 16×16 pixels were used with an overlap of 50% to obtain the velocity field (space resolution $\delta x = 0.90$ mm). One hundred pairs of independent images were captured for each tested configuration with a sampling frequency of 5 Hz.

For one specific location ($X=100$ mm), the space resolution and the statistical convergence were improved by reducing the images to 52 mm × 52 mm (space resolution $\delta x = 0.20$ mm) and acquiring 1000 pairs of independent images (the RMS error of the time-averaged velocity for a 95% confidence interval is reduced to 2.5% for the worst case).

3. Results and discussion

The primary objective is to identify the main differences in mean flow characteristics due to the rounding of the edge between the roof and the rear window of an Ahmed body with a slant angle of 25°. Figs. 3 and 4 show the drag C_d and lift C_l coefficients, respectively, versus the Reynolds number based on the Ahmed body length Re_L for the sharp- and rounded-edge configurations. Fig. 3 shows that for both configurations, the drag coefficient decreases as the Reynolds number increases but tends to an asymptotic value of $C_d=0.38$ and $C_d=0.34$ for the sharp- and rounded-edge configurations, respectively. This illustrates that, for the sharp-edge configuration, the flow does not fully reach the Reynolds number independence for the Reynolds number range tested. The drag coefficient for the sharp-edge configuration is overestimated by 30% compared to literature values (Ahmed et al., 1984). The same observation was reported in the study by
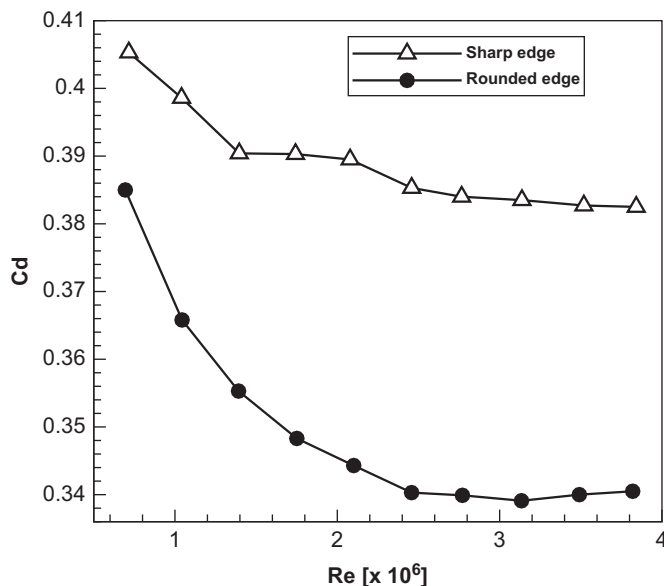

Fig. 3. Drag coefficient versus Reynolds number based on the Ahmed body length for the sharp- and rounded-edge configurations.
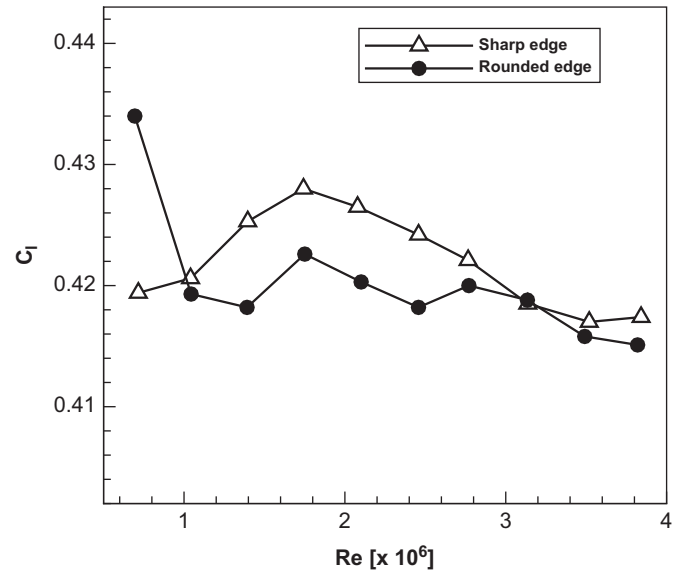

Fig. 4. Lift coefficient versus Reynolds number based on the Ahmed body length for the sharp- and rounded-edge configurations.

Conan et al. (2011) and could be due to a high sensitivity on the separation due to the sharpness of the roof/rear window edge connection. However, the drag coefficient is 10% smaller for the rounded-edge case than for the sharp-edge one, showing the effect of the separation on the drag for identical operating conditions. Moreover this reduction of 10% has also been observed by suppressing the separation on the rear window using a flow control device (Aubrun et al., 2011). Despite this difference in the drag coefficient, the lift coefficient C_l is not really modified (Fig. 4), since for $Re_L > 1 \times 10^6$ the maximum of lift difference is 1.5% between the two configurations. This result will be further discussed in the next section.

3.1. Flow topology on the rear part of the Ahmed body

To explain discrepancies between the two configurations, the modifications in the flow topology on the rear window due to the rounding of the edge were studied with the help of friction line visualizations, static pressure coefficient distributions and PIV velocity fields (Figs. 5–7).

Friction line visualizations on the rear window are shown in Fig. 5 for both configurations and are superimposed with static pressure coefficient distributions. In the sharp-edge configuration, a mostly attached flow is maintained as observed by Lienhart and Becker (2003). The separation line is superimposed with the sharp edge and the reattachment line AB is elliptic-shaped and delimits a 3D closed separation bubble. On the middle plane the separation is maximum and the mean reattachment is located at $X/l = 0.73$. In the rounded-edge configuration in contrast, no separation is visible on the rear window: the friction lines on the central part of the window are aligned with the streamwise direction. These results are confirmed with the streamline patterns of the velocity field in the plane of symmetry (Fig. 7). The closed separation is clearly identified on the rear window for the sharp edge configuration while the flow is fully attached for the rounded edge case.

The comparison between the two flow configurations in Fig. 5 shows the influence of the separation bubble on the wall pressure distribution over the rear window. As observed by Lienhart and Becker (2003), the footprint of the separation bubble on the pressure distribution is clearly visible for the sharp edge configuration since isocontours of the static pressure coefficient are
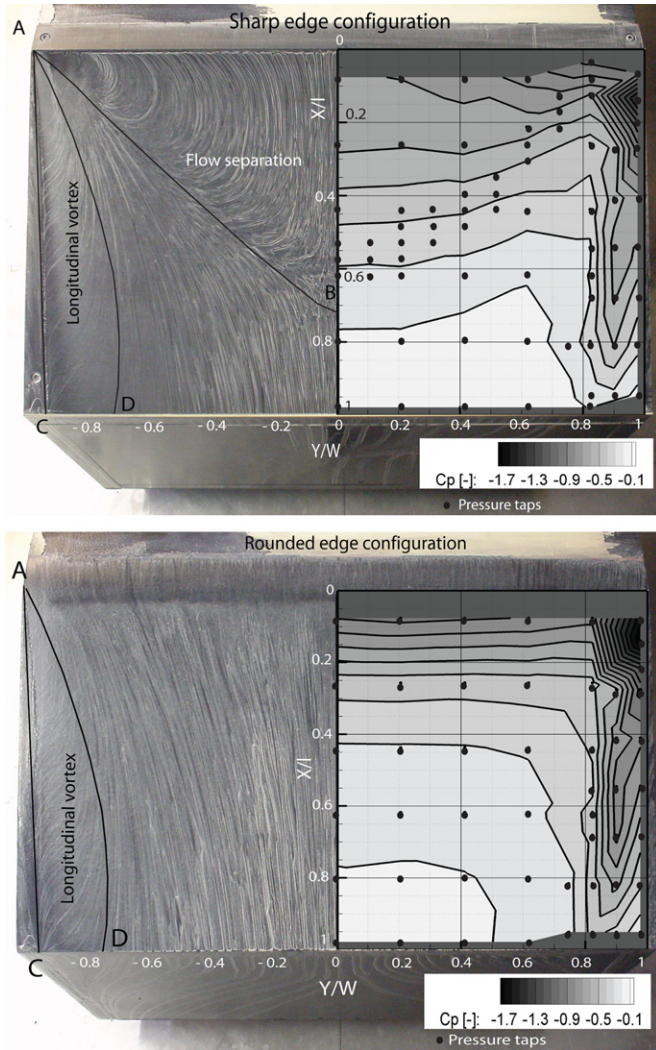
Fig. 5. Wall pressure coefficient distributions combined with surface flow visualizations on the rear window for the sharp-edge (top) and the rounded-edge (bottom) configurations. Black circles show the pressure tap locations, $Re_L = 2.2 \times 10^6$.
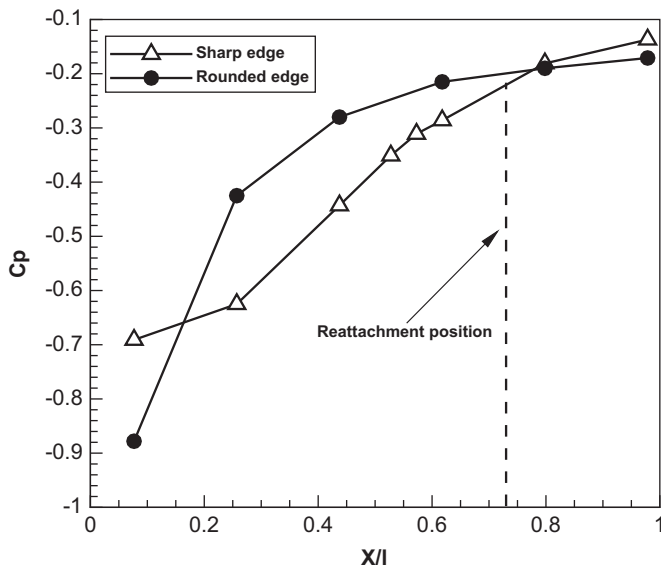

Fig. 6. Wall pressure coefficient distributions along the rear window for the sharp- and rounded-edge configurations, $Re_L = 2.2 \times 10^6$.
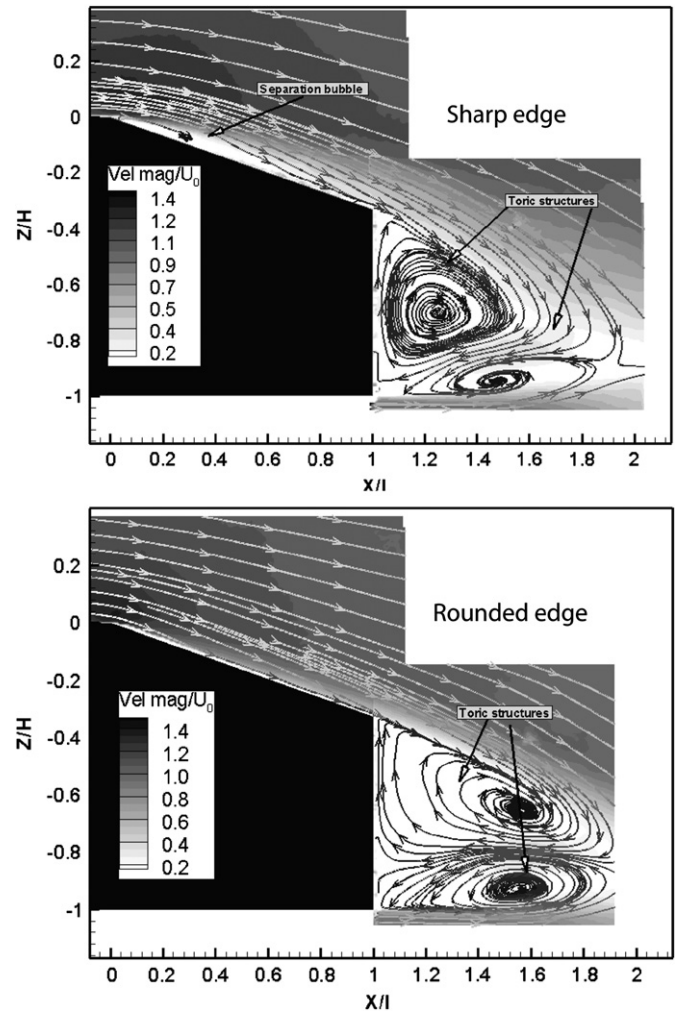

Fig. 7. Mean velocity magnitude fields in the vertical middle plane on the rear window and at the rear base of the Ahmed body for the sharp-edge (top) and the rounded-edge (bottom) configurations, $Re_L = 2.2 \times 10^6$.

correlated with the elliptic shape of the separation bubble. Fig. 6 presents the static pressure coefficient profile along the middle line of the rear window for both flow configurations. It can be clearly seen that a large part of the central region of the rear window is subjected to lower static pressure when the separation bubble exists (sharp-edge config.). For the rounded-edge configuration, the absence of a separation close to the roof/slant connection leads to a higher curvature of the streamlines (see Fig. 7), so that the flow is locally accelerated and the static pressure is lower for $X/l < 0.15$. Obviously, since the flow is fully attached in this configuration, the static pressure increases for $X/l > 0.15$ and becomes higher than it is when the flow separates.

Fig. 5 also shows the signature of the longitudinal vortical structures, which are generated by the convergence and rolling up of the flow coming from the roof and from the sides of the body (Gilliéron et al., 2010), through the appearance of the attachment line AD and the separation line AC. They are accompanied by secondary and tertiary vortical structures (the latter are not visible on the present visualizations but were observed by Krajnovic and Davidson, 2005, for a lower Reynolds number of $Re_L = 0.7 \times 10^6$) confined between the separation line AC and the side edge. These longitudinal vortical structures lead to a low pressure within their cores, which generate an under-pressure signature on the rear window (Fig. 5). Since the core location moves farther from the rear window with the streamwise distance,

the under-pressure is expected to decrease with this distance. The friction lines, as well as the wall pressure, in the vicinity of these vortical structures do not seem to be modified by the presence of the separation bubble.

Finally, the mean velocity magnitude fields in the symmetry plane (Fig. 7) show that the main difference between the two configurations is located at the rear base, since the topology of the toric vortices is more symmetrical for the rounded-edge case and their vortical centers, which are characterized by a low pressure core, are farther from the rear base. Similar results were observed in cases of separation suppression using flow control (Aubrun et al., 2011) and could be attributed to the substantial modification of the shear layer thickness coming from the rear window. The modification of the near rear wake without separation on the rear window is indirectly responsible for the drag difference observed in Fig. 3. Indeed, it is clearly observed that the suppression of the separation bubble does not affect enough the wall pressure distribution on the rear window to impact on the generated lift (see Fig. 4). Since the rear base cannot contribute to the lift, this result indicates that the contribution of the rear window to the aerodynamic loads is globally unchanged and that the reason for the drag reduction should be attributed to the near rear wake modification. In addition, the fact that the low static pressure core of the toric vortices is farther from the rear base, when the flow is fully attached on the rear window, leads to a higher static pressure on the surface (Leclerc, 2008) so that the pressure drag contribution of the rear base is reduced. This was more particularly emphasized by Aubrun et al. (2011) using flow control.

3.2. Longitudinal vortical structures

In order to study the influence of the presence of the recirculation bubble on the longitudinal vortical structures, the space coordinates of their mean and instantaneous centers were tracked by using the maximum of the Q-criterion (Hunt et al., 1988). For both test cases, velocity fields obtained by PIV on YZ planes were used to compute Q_{mean}, the dimensionless 2D Q-criterion deduced from the mean velocity fields, and the instantaneous dimensionless 2D Q-criteria Q_{inst} deduced from the instantaneous velocity fields:

$$Q_{mean}(X,Y,Z) = \left(-\left(\frac{\partial \overline{V}}{\partial Y}\right)^2 - \frac{1}{2}\frac{\partial \overline{V}}{\partial Z}\frac{\partial \overline{W}}{\partial Y} \right)\frac{S}{U_0^2} \quad (2)$$

$$Q_{inst}(X,Y,Z,t) = \left(-\left(\frac{\partial V}{\partial Y}\right)^2 - \frac{1}{2}\frac{\partial V}{\partial Z}\frac{\partial W}{\partial Y} \right)\frac{S}{U_0^2} \quad (3)$$

With S the model cross area and U,V and W the three velocity components:

$$U(X,Y,Z,t) = \overline{U}(X,Y,Z) + u'(X,Y,Z,t) \quad (4)$$

$$V(X,Y,Z,t) = \overline{V}(X,Y,Z) + v'(X,Y,Z,t) \quad (5)$$

$$W(X,Y,Z,t) = \overline{W}(X,Y,Z) + w'(X,Y,Z,t) \quad (6)$$

Fig. 8 shows the coordinates of the Q_{mean} maximum along the rear window and the rear part of the body for both configurations. Since the Q-criterion is maximum at the center of a vortical structure (Scanaro, 2008), Fig. 8 is expected to show the coordinates of the longitudinal vortex mean center. The structure axis is straight on the rear window with an angle from the slanted surface of $\alpha = 6.2°$ for the sharp-edge case and $\alpha = 6°$ for the rounded-edge one (with an uncertainty due to PIV space resolution of $0.3°$). The vortical structure axis is deviated at the end of the rear window ($X/l = 1$) by an angle $\theta = 14.7°$ for the sharp-edge case and $\theta = 13.3°$ for the rounded-edge one. The vortical structure axis also presents
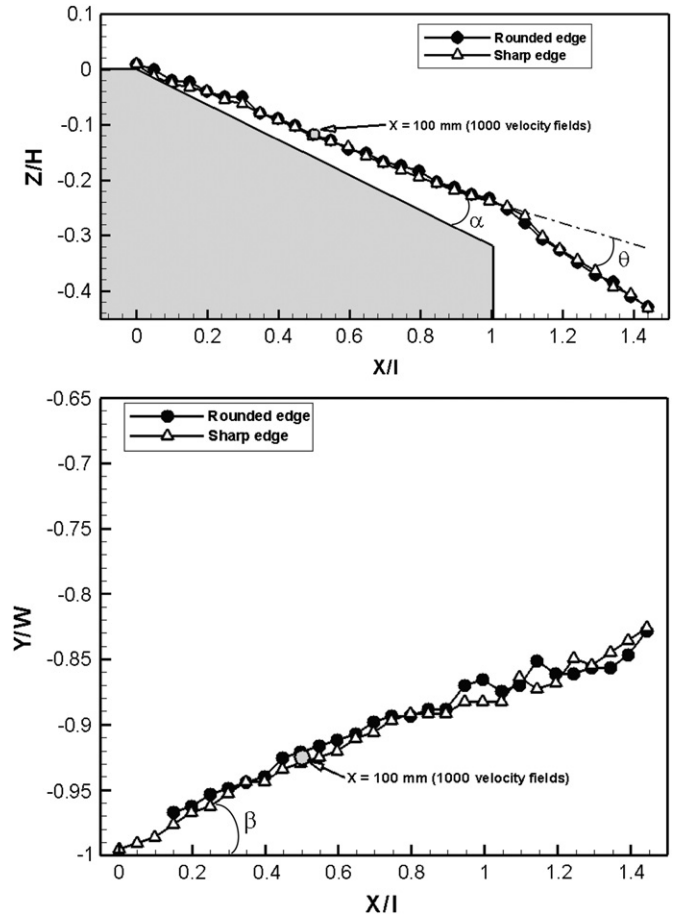

Fig. 8. Mean vertical (top) and transverse (bottom) coordinates of the center of the longitudinal vortical structure for the sharp- and the rounded-edge configurations, $Re_L = 2.2 \times 10^6$.

an angle from the vertical side of the body $\beta = 6.2°$ for the sharp-edge case and $\beta = 6.6°$ for the rounded-edge one. These values are in agreement with previous work on similar configurations by Lehugeur (2007) and Roumeas et al. (2008). The comparison between the two configurations shows that the presence of the closed separation bubble on the rear window does not impact the mean location of the longitudinal vortical structures, which develop on both sides of the rear window.

Fig. 9 shows the streamwise vorticity with a log-scale distribution deduced from the mean velocity fields through the longitudinal vortices at a distance $X/l = 0.5$ for both configurations. At this position, the discrepancy of static pressure on the rear window between the two configurations is relevant (see Figs. 5 and 6). The locations of each instantaneous Q_{inst} maximum are shown on the graph with black dots and the location of Q_{mean} maximum is shown by a black circle. The vorticity distribution is used here as it provides a better visualization of the rolling motion of the structure than the Q-criterion which is most representative at the vortical center. No major difference is visible on the global vorticity distribution between the two cases, even if the vortical structure for the rounded-edge configuration is located slightly closer to the wall and fluctuates a little more around its mean position. The location of the Q_{mean} maximum, indicating the mean vortical center, presents a discrepancy of 2 mm between the two configurations. The distribution of the instantaneous vortical center locations presents a scatter of 1–1.5 mm from the mean location for the sharp-edge and the rounded-edge configurations, respectively. These results demonstrate that the longitudinal vortical structure is spatially very stable in both cases.
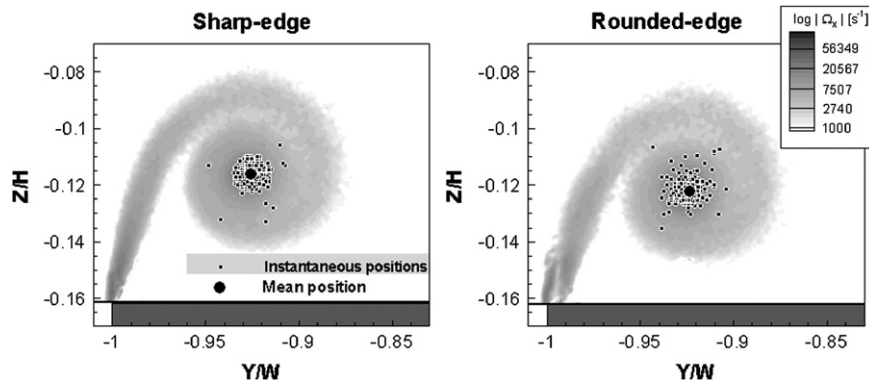
Fig. 9. Mean streamwise vorticity distribution at a distance $X/l = 0.5$ on the rear window for the sharp-edge (left) and the rounded-edge (right) configurations, $Re_L = 2.2 \times 10^6$.
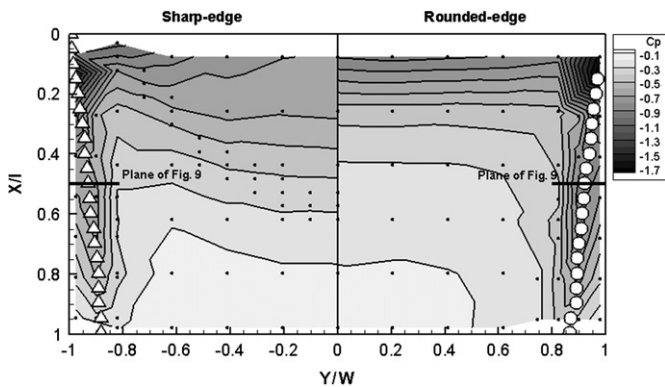

Fig. 10. Mean pressure coefficient distributions on the rear window for the sharp-edge (left) and the rounded-edge (right) configurations. Black circles show the pressure tap locations. White triangles and white circles show the longitudinal vortices positions for the sharp edge and the rounded edge configurations, respectively, $Re_L = 2.2 \times 10^6$.

Fig. 11. RMS pressure coefficient distributions on the rear window for the sharp-edge (left) and the rounded-edge (right) configurations. Black circles show the pressure tap locations. White triangles and white circles show the longitudinal vortices positions for the sharp edge and the rounded edge configurations, respectively, $Re_L = 2.2 \times 10^6$.
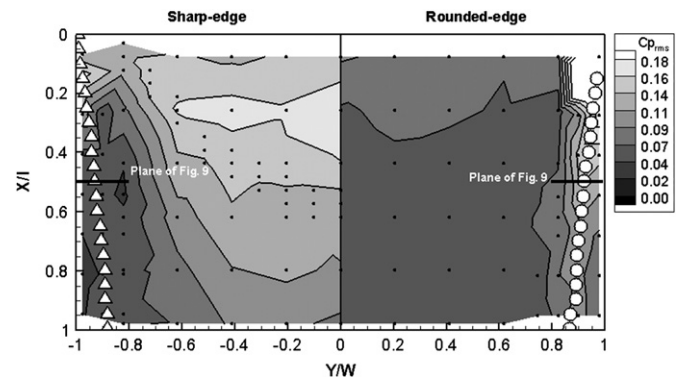
On the other hand, the Q_{mean} maxima are very different since $Q_{mean}^{max} = 71{,}000$ and $25{,}000$ for the sharp-edge and the rounded-edge configurations, respectively. Computing the ensemble average and the standard deviation of the instantaneous Q-criterion maxima Q_{inst}^{max} for both configurations gives the same conclusion: $\langle Q_{inst}^{max} \rangle = 198{,}000$ for the sharp-edge case and $107{,}000$ for the rounded-edge one. The associated standard deviations are $\sigma(Q_{inst}^{max}) = 116{,}000$ and $47{,}000$ and the Q_{inst}^{max} fluctuation intensities are then 59% and 44%, respectively. This indicates that the larger fluctuations of the instantaneous positions of the longitudinal vortices in the rounded edge case do not contribute to their weaker vorticity. Moreover, it shows that the vortical structure intensity is higher but fluctuates less spatially for the sharp-edge configuration. One explanation of this feature can be found by studying the mean and fluctuating wall-pressure distributions on the overall rear window (Figs. 10 and 11). The pressure distribution is globally lower on the rear window with the presence of the separation bubble (sharp-edge case). Consequently, the suction effect on the rear window, which is responsible for the vortical structure formation, is higher, leading to stronger vortical structures. On the other hand, the presence of the separation induces higher pressure fluctuations on the rear window, leading to higher fluctuations in the vortex strength (defined as either vorticity or Q-criterion). To conclude, the flow and pressure disturbances generated by the 3D separation bubble on the rear window are not strong enough to significantly modify the longitudinal vortical structure location but are strong enough to modify its intensity.

4. Conclusion

An experimental characterization of the flow in the near-wake of the Ahmed reference model with a slant angle of 25° has been carried out. In order to analyze the effect of the suppression of the separation on the rear slant, two distinct models have been used, the first one having a sharp edge at the roof/rear slant connection and the second one having a rounded edge which prevents flow separation on the rear slant. Aerodynamic loads, wall pressure distribution, friction line visualizations and PIV velocity fields have been performed to compare the two flow configurations.

The results show that the drag level is 10% smaller without flow separation on the rear window while the lift component of aerodynamic loads is unchanged. This difference is explained by certain modifications in the flow topology. Without flow separation, the central part of the rear window shows a higher level of static pressure which neither significantly impacts on the rear window pressure drag contribution nor on the global lift. Nevertheless, due to a complex interaction between the rear window and the rear wake flow, the vortical center of the wake toric vortices, associated with a low pressure core, are located farther from the rear base which mainly contributes to the weaker drag level.

Wall pressure distributions as well as skin friction line visualizations did not exhibit any major differences in the vicinity of the longitudinal vortical structures. These structures were then more precisely analyzed using PIV velocity fields in a cross section. Results show that the absence of the flow separation on the rear window does not impact the mean location of the

longitudinal vortices; nor were any major differences observed on the global vorticity distribution except that the vortical center intensity is lower. This observation has been confirmed by analyzing instantaneous vorticity distributions which showed moreover that vorticity fluctuations (or Q-criterion) are lower without separation. One explanation for this result is that the pressure distribution is globally higher on the rear window without separation and thus the suction effect responsible for the longitudinal vortical structures formation is weaker. Furthermore, flow separation induces high pressure fluctuations on the rear window which can explain higher fluctuations in the vortex strength. In both cases, the instantaneous locations of the vortical center are concentrated around their mean location, proving that the longitudinal vortical structures are spatially very stable.

This study thus provides a comparison between separated and non-separated configurations for an Ahmed reference model with a 25° slanted rear window. It thereby constitutes a reference database which can be used with a view to the rear window separation control associated with the development of control devices.

References

Ahmed, S.R., Ramm, G., Faltin, G., 1984. Some salient features of the time averaged ground vehicle wake. SAE Technical Paper Series 840300, Detroit.

Anne-Archard, D., Du Colombier, D., Boisson, H., Herbert, V., 2006. Analyse des enduits de visualisation pariétale utilisés en aérodynamique. In: 41ème Colloque National du Groupe Français de Rhéologie, 18–20 octobre 2006, Cherbourg, France.

Aubrun, S., McNally, J., Alvi, F., 2011. Separation flow control on a generic ground vehicle using steady microjet arrays. Experiments in Fluids 51, 1177–1187.

Benedict, L.H., Gould, R.D., 1996. Towards better uncertainty estimates for turbulence statistics. Experiments in Fluids 22, 129–136.

Bergh, H., Tijdeman, H., 1965. Theoritical and Experimental Results for the Dynamic Response of Pressure Measuring Stems. Netherlands National Aero- and Astronautical Research Institute, Report NLR-TR F.238.

Conan, B., Anthoine, J., Planquart, P., 2011. Experimental aerodynamic study of a car-type bluff body. Experiments in Fluids 50, 1273–1284.

Gilliéron, P., Kourta, A., 2008. Automobile et environnement: contribution de la recherche aérodynamique à la réduction des gaz à effet de serre. Mécanique & Industries 9, 519–531.

Gilliéron, P., Leroy, A., Aubrun, S., Audier, P., 2010. Influence of the slant angle of 3D bluff bodies on longitudinal vortex formation. Journal of Fluids Engineering 132, 051104.

Hunt, J.C.R., Wray, A.A., Moin, P., 1988. Eddies, streams and convergence zones in turbulent flows. In: Proceedings of the Summer Programm N89-24555. Center for Turbulence Research, pp. 193–208.

Krajnovic, S., Davidson, L., 2005. Flow around a simplified car. Part 1: large Eddy simulation. Part 2: understanding the flow. Journal of Fluids Engineering 127, 907–928.

Leclerc, C., 2008. Réduction de trainée d'un véhicule automobile simplifié à l'aide du controle actif par jet synthétique. Thèse de Doctorat. Institut de Mécanique des Fluides de Toulouse.

Lehugeur, B., 2007. Caractérisation et controle des structures tourbillonnaires longitudinales en aérodynamique automobile. Thèse de Doctorat. Université Pierre et Marie Curie.

Lienhart, H., Becker, S., 2003. Flow and turbulence structure in the wake of a simplified car model. In: SAE World Congress, Detroit, Michigan, SAE 2003-01-0656.

Roumeas, M., Gilliéron, P., Kourta, A., 2008. Separated flows around the rear window of a simplified car geometry. Journal of Fluids Engineering 130, 1–10.

Serre, E., et al., On simulating the turbulent flow around the Ahmed body: a French-German collaborative evaluation of LES and DES. Computers & Fluids, http://dx.doi.org/10.1016/j.compfluid.2011.05.017, in press.

Scanaro, F., 2008. Three dimensional measurements by tomographic PIV. Post-processing of numerical and experimental data. Von Karmann Institut Lecture Series.

Vino, G., Watkins, S., Mousley, P., Watmuff, J., Prasad, S., 2005. Flow structures in the near-wake of the Ahmed model. Journal of Fluids and Structures 20, 673–695.